www.sciencemag.org/content/353/6306/1406/suppl/DC1

Supplementary Materials for

Tomography reveals buoyant asthenosphere accumulating beneath the Juan de Fuca plate

William B. Hawley,* Richard M. Allen, Mark A. Richards

*Corresponding author. Email: whawley@seismo.berkeley.edu

Published 23 September 2016, *Science* **353**, 1406 (2016)
DOI: 10.1126/science.aad8104

This PDF file includes:

Materials and Methods

Data

For this study, we have compiled a dataset of teleseismic direct- and core-phase P-wave arrivals at stations on the Juan de Fuca plate and across the western United States. The data were provided by more than 1300 stations (Fig. S1)—including 90 offshore—from the following networks: Cascadia Initiative (CI), Plate Boundary Evolution and Physics at an Oceanic Transform Fault System (X9), Neptune Canada (NV), the EarthScope Transportable Array (TA), two EarthScope Flexible Array deployments (FACES and Mendocino), Global Seismographic Network (IU), GEOSCOPE (GEO), United States National Seismic Network (USNSN), ANZA Regional Network (ANZA), Berkeley Digital Seismic Network (BDSN), Cascade Chain Volcano Monitoring Network (CC), COLZA/OSU, DELTA LEVY Northern California, Montana Regional Seismic Network (MRSN), Northern California Seismic Network (NCSN), Western Great Basin/Eastern Sierra Nevada Network (NN), Southern California Seismic Network (SCSN), University of Oregon Regional Network (UO), University of Utah Regional Network (UURN), Pacific Northwest Regional Seismic Network (PNSN), Yellowstone Wyoming Seismic Network (WY). Our data were collected from 321 seismic events ranging in magnitude from 5.5 to 7.5 that occurred between January 2007 and July 2013 (Fig. S2). For each event, we use only data from stations that were between 30 and 80 degrees from the epicenter.

Noise Removal

Seismic stations on the ocean floor provide a new and valuable scientific resource, even when used to augment data from land-based stations. The noise characteristics of the two types of stations, however, can be very different. For OBS stations, the noise is generally derived from wind and waves, both by direct forcing at longer periods and by coupling to elastic waves in the earth at shorter periods (*37*).

In order to filter out this noise, we analyzed the P-wave arrival signal in a number of bands, including bands that have been published as being suitable for observing teleseismic body waves [e.g. Lewis and Dorman (*38*)]. Much of the intermediate frequency range—about 0.5 to 2 Hz; frequencies that produce the best teleseismic arrivals on land-based stations—is dominated by noise in the ocean stations (Fig. S3). Cross-correlating arrivals requires picking the arrival at each station in the same frequency band. We placed priority on obtaining data from the OBS stations, while still ensuring we obtained reliable data from the land-based stations. We determined that using the relatively low-frequency and narrow passband from 0.08 to 0.11 Hz (about 9 to 12.5 seconds period) resulted in the clearest body wave arrivals for the OBS stations. Two additional frequency bands were used for data from the land-based stations (0.02 to 0.1 Hz and 0.8 to 2.0 Hz), but did not provide useful data from ocean-bottom stations.

Inversion Method

After filtering, we follow the inversion method as in Obrebski *et al*. 2010 (*11*). Each arrival was picked manually and cross-correlated with each other waveform for that event, which results in a dataset of relative travel-time delays (*39*). For all three bands, those records with a cross-correlation coefficient less than 0.9 were discarded. The resulting dataset was comprised of 61,559 relative P-wave travel-time delays.

The tomographic inversion technique we employ uses finite-frequency sensitivity kernels to account for wavefront healing and scattering. We use paraxial kernel theory to calculate, for each frequency band used to pick P arrivals, the frequency- and depth-dependent sensitivity around the infinitely thin ray that defines the path from seismic source to receiver (*40–42*).

We prescribe a model domain as a spherical cap that extends from 27°N to 51°N and 133°W to 101°W, and from the surface to 2500km depth. In both horizontal directions and the vertical direction there are 65 nodes. The model box is larger than the region in which we expect to have good resolution in all directions. We incorporate station corrections (Fig. S1) to account for delays common to each station owing to the geology directly beneath that station. This correction prevents crustal delays from smearing down into the mantle, which is especially important for our ocean bottom stations. Event corrections (Fig. S2) are also included in the inversion. The finite-frequency inversion means there is no need for smoothing, but it does require damping; we use LSQR to iterate to a final model. Slices through the model are provided in Fig. S4.

Additional inversions were performed with different station correction damping terms; these models are shown in Fig. S5. We show three inversions: one for which the station corrections are highly damped, which results in almost all of the travel-time delay for each station to be attributed to the mantle (Fig. S5A–C), an intermediate damping that is presented in the manuscript (Fig. S5D–F), and one with negligible damping, which allows for the largest individual station corrections supported by the data. Further reduction of the damping results in negligible changes to the station corrections. These models demonstrate that the low-velocity feature we interpret is a robust feature of the model across the range of station correction terms, and cannot be attributed exclusively to shallow slow structure being incorrectly mapped to depth.

Resolution Tests

We input specific geometries motivated by our interpretation of the model to test its resolution. Fig. S6 shows that introducing only high-velocity anomalies does not induce a low-velocity artifact that might account for our observed low-velocity feature. Fig. S7 demonstrates that the observed limited westward extent of the low-velocity roll in CASC16-P is not an artifact of the inversion. Fig. S8 shows various configurations of low-velocity features beneath the subducting slab. Figs. S8A–B show that a weak low-velocity feature beneath the slab that extends to the transition zone is not recovered well at greater depths, however the strength of the signal beneath the hinge of the subducting slab is weaker than the feature in CASC16-P. Figs. S8C–D show that a stronger low-velocity feature beneath the slab matches the strength of the signal of that seen in CASC16-P, but is also resolved down to 400km, in contrast with CASC16-P. Figs. S8E–H show low-velocity features that extend only to 150km and 200km appear to extend to 250km and 400km respectively, and match CASC16-P reasonably well.

Two checkerboard resolution tests are shown in Figs. S9–S12, which show good recovery of structures that are approximately 85km and larger down through the transition zone throughout the majority of the model domain.

Scaling Calculations for Flow in the Low-viscosity Channel and Accumulation Zone

Channel flow driven by plate motion and resisted by channel buoyancy: The conditions under which the buoyancy of the low-density, low-viscosity channel material can effectively resist being advected downward into the mantle by the subducting slab can be understood as a simple competition between Couette-type flow driven by the slab and Poiseuille-type flow driven by the buoyancy of this material. In the coordinate system indicated in Fig. 3, the Couette flow velocity in the channel parallel to the slab motion is given by $v_c = v_0(y/h)$ where the y coordinate is zero at the bottom of the channel and h at the top. The buoyancy-driven Poiseuille flow resisting this motion is given by $v_p = -\frac{\Delta\rho g sin(\theta)}{2\mu_l} y(y-h)$ where the negative sign indicates motion opposing the plate-driven flow. The approximate condition for accumulation of the buoyant layer material beneath the subduction zone is that the integral of the Poiseuille flow velocity over the channel depth $(y = 0, h)$ is larger than or comparable to the integrated Couette flow, or

$$\frac{\Delta\rho g sin(\theta) h^2}{6 v_0 \mu_l} \gtrsim 1$$

Gravity flow of accumulated channel material resisted by overlying plate-driven advection: The above condition describes the conditions under which low-density, low-viscosity channel material may begin to accumulate beneath the subduction zone. However, this calculation does indicate how much material (what thickness *H*) can accumulate until its own buoyancy causes it to spread horizontally as fast as it can accumulate. The latter condition is obtained by setting the gravity flow velocity approximately equal to the overlying horizontal plate motion. Following the analysis of Feighner and Richards, 1995 (*25*) for a blob or "pancake" of thickness *H* of low-density, low-viscosity material spreading beneath a plate, and being resisted by a much higher-viscosity surrounding mantle, we can approximate the horizontal gravity force acting over an area *Dh* as $\Delta\rho g H^2 D$, where *D* is the surface area of the accumulated blob of channel material. (In our case *D* and *H* are, in fact, comparable, but this is of no consequence as *D* drops out of the calculation below.) The retarding viscous force is given by $\mu_m v_g D$, where v_g is the horizontal gravity flow velocity. Requiring that the gravity flow velocity not exceed the overlying plate velocity ($v_g \lesssim v_0$) as a condition for maintaining a roll of thickness *H* yields

$$\frac{\Delta\rho g H^2}{v_0 \mu_m} \lesssim 1$$

We note that the first condition above involves the relatively low channel viscosity μ_l, whereas the second condition involves the relatively high underlying mantle viscosity μ_m. This is consistent with our conceptual model in which the sublithospheric channel thickness is smaller (perhaps much smaller) than the dimension of the accumulated material beneath the subduction zone, that is, *h* < *H*. In fact, these two conditions together reveal that the ratio of the mantle viscosity and the layer viscosity is proportional to the ratio of the square of the accumulation zone thickness and the layer thickness, or

$$\frac{H^2}{h^2} \sim \frac{\mu_m}{\mu_l}$$

Two plots that explore the relationships between the thicknesses and the relevant viscosities are shown in Fig. S13.

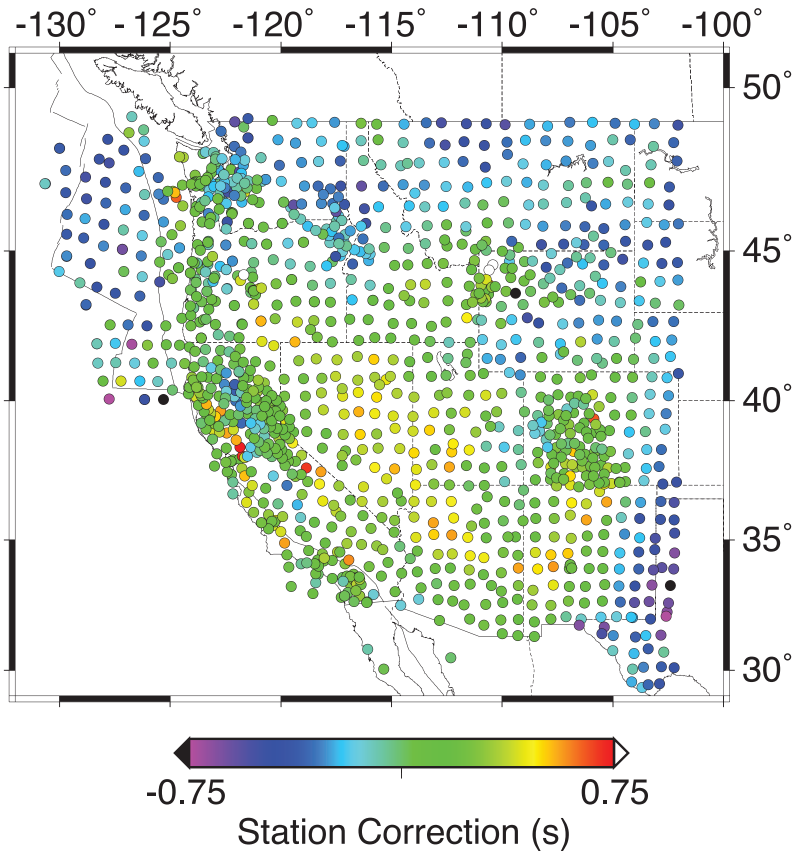

Fig. S1.
Circles are stations used in the inversion, with color showing the correction determined in the inversion to account for delays common to a station for all arrivals. This correction helps to account for shallow structure beneath each station.

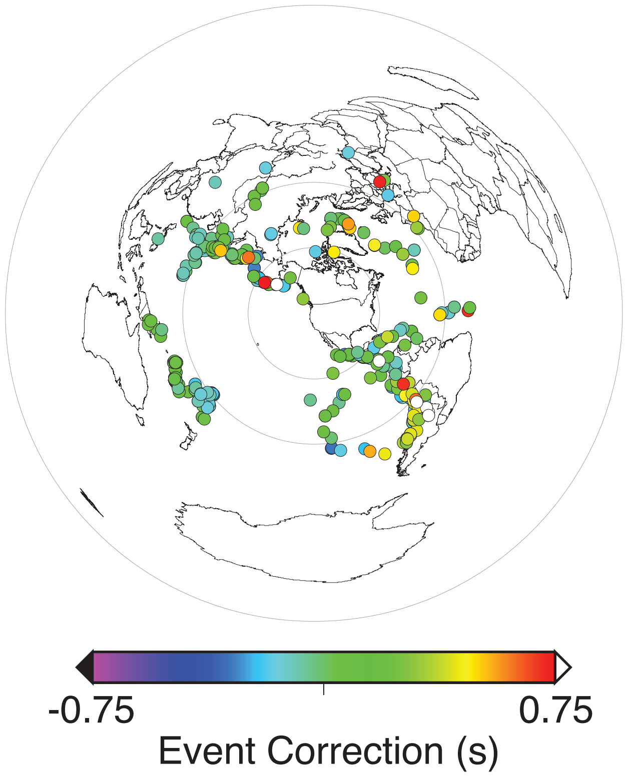

Fig. S2.
Circles show events used in the inversion, with color showing the event correction determined in the inversion common to arrivals for a single event. This helps account for structure outside the model domain. Two reference circles are plotted at 30° and 60° centered on 44°N, –121°E, in central Oregon.

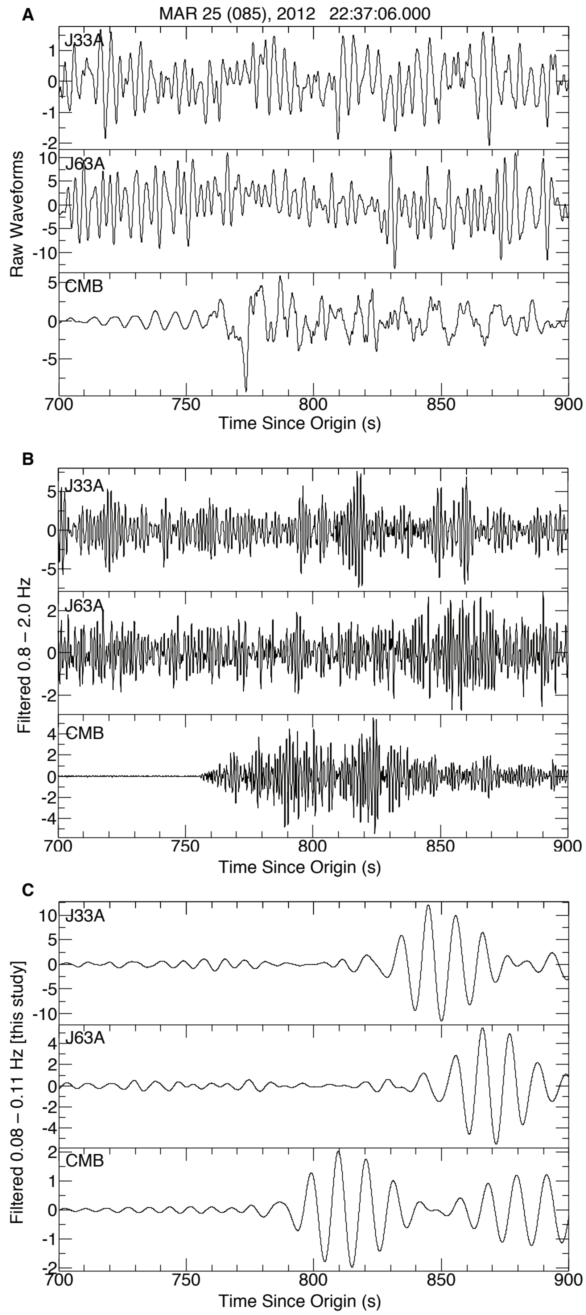

Fig. S3.

(**A**) Raw waveforms from a shallow OBS (J33A, 348m depth), a deep OBS (J63A, 2882m depth), and a land-based station (CMB) showing the P arrival from a M7.1 event in Chile. (**B**) The same waveforms filtered 0.8 – 2.0 Hz, a common filter (*37*) for teleseismic P imaging studies onshore. The two OBS show no clear P arrival. (**C**) The primary filter band used in this study, 0.08 – 0.11 Hz, shows clear and similar arrivals on all three stations.

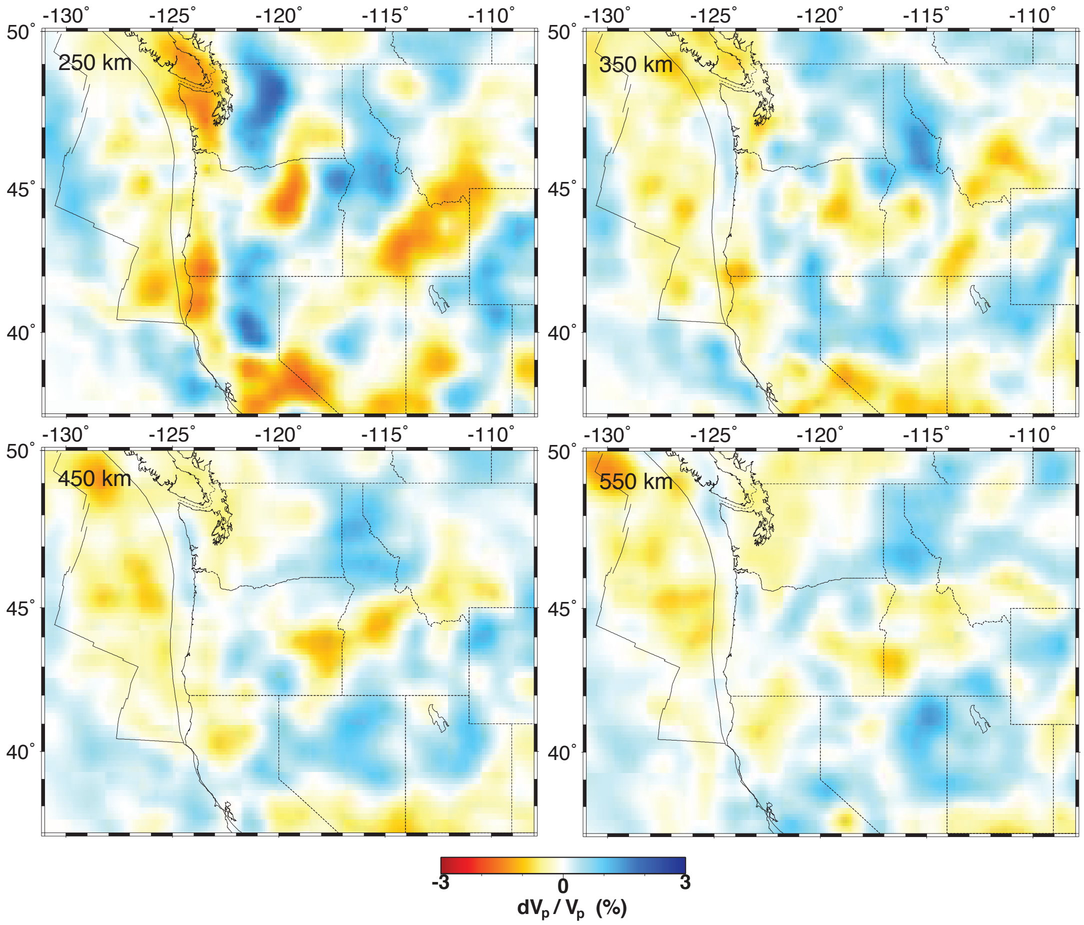

Fig. S4.
Horizontal slices at constant depth, labeled in the upper left corner, through CASC16-P.

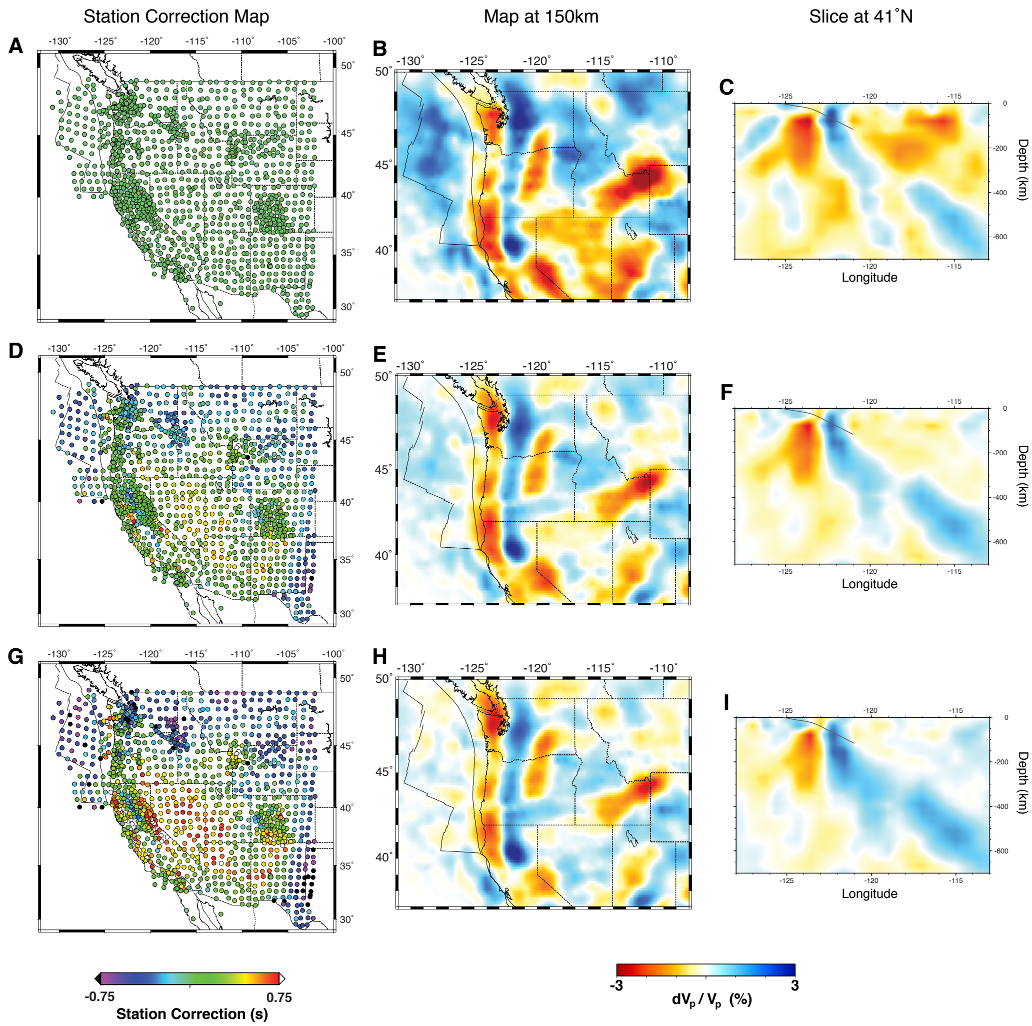

Fig. S5.

Three inversions with various station correction parameters. (**A–C**) Inversion result where the station corrections are highly damped, resulting in small station corrections and more of the signal being pushed into the (deeper) velocity model. (**A**) A map of station corrections determined in the inversion. (**B**) A horizontal slice at 150km depth of the same inversion. (**C**) A vertical slice through the same model at 41°N. (**D–F**) As with (**A–C**), but with less damping of station corrections, thus allowing for larger station corrections. This is the model we have used for interpretation. (**G–I**) As with (**A–C**), but negligible damping; this allows for the largest individual station corrections that the data can support. Despite more of the travel-time delay being attributed to the geology directly beneath the station, i.e., accommodated in the station correction, the major geologic features observed in the velocity model remain strong elements in the model. Further reduction in the damping of the station correction terms results in negligible changes to the values of the corrections, meaning that the station correction terms have absorbed as much signal as they are able in the inversion shown in (**G–I**).

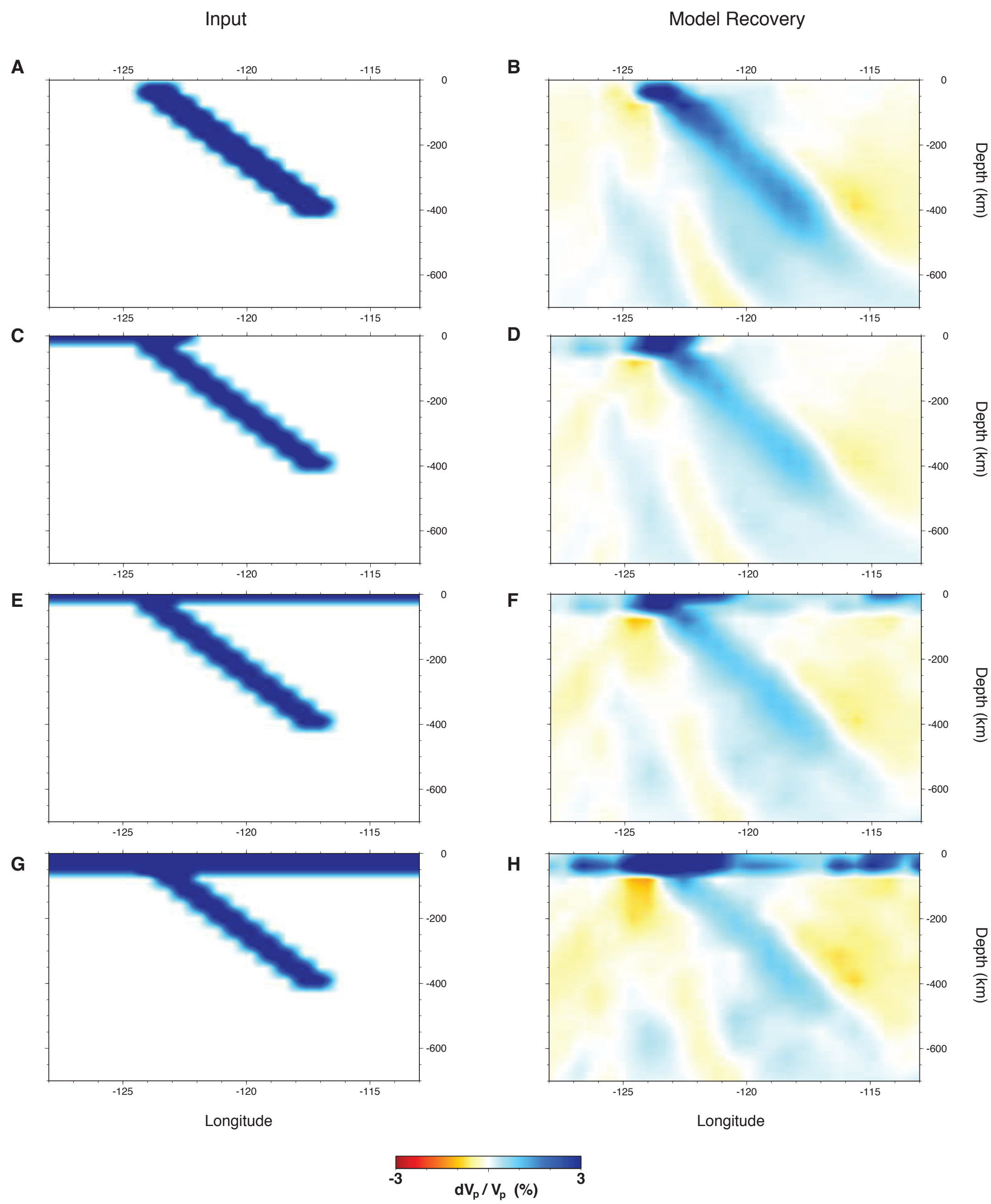

Fig. S6.

Synthetic models that include only high-velocity anomalies are unable to produce artifacts of the amplitude observed in CASC16-P, as in Fig. 2. (**A–B**) A 100km-thick, +6% high-velocity feature was used as an input synthetic velocity model. (**C–D**) An 80km-thick, +4% slab is attached to a 20km-thick lithospheric lid that extends to the west. (**E–F**) An 80km-thick, +4% slab is attached to a 20km-thick lithospheric lid that extends to the east and the west. (**G–H**) An 80km-thick, +4% slab is attached to a 60km-thick lithospheric lid that extends to the east and the west. All configurations generate low-velocity artifacts that are low-amplitude, small scale, and not continuous.

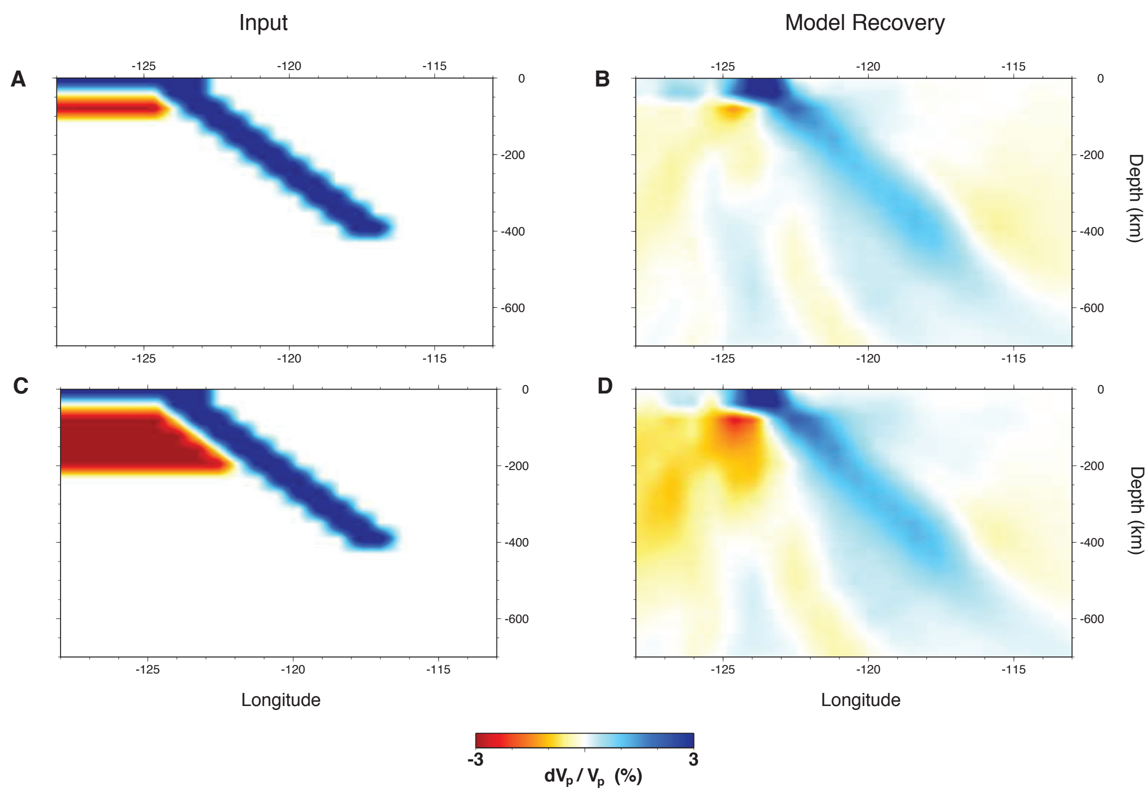

Fig. S7.

Synthetic models test our resolution of the western edge of the sub-slab low velocities. (**A**) An 80km-thick, +4% slab is connected to a lithospheric lid that extends to the east and the west. A 40-km thick, –4% horizontal feature lies under the lithospheric lid to the west. (**B**) Recovery shows that the strongest low-velocity signal comes from the eastward edge of the low-velocity feature, but it is low in amplitude, and low velocities are continuous well to the west, in contrast with CASC16-P. (**C**) A similar 80km-thick, +4% slab is connected to a lithospheric lid that extends to the west. A 160km-thick, –3% region lies under the lithospheric lid. (**D**) The strongest low-velocity recovery is in the slab hinge, but low velocities are pervasive under the lithospheric lid down to the transition zone, in contrast with CASC16-P.

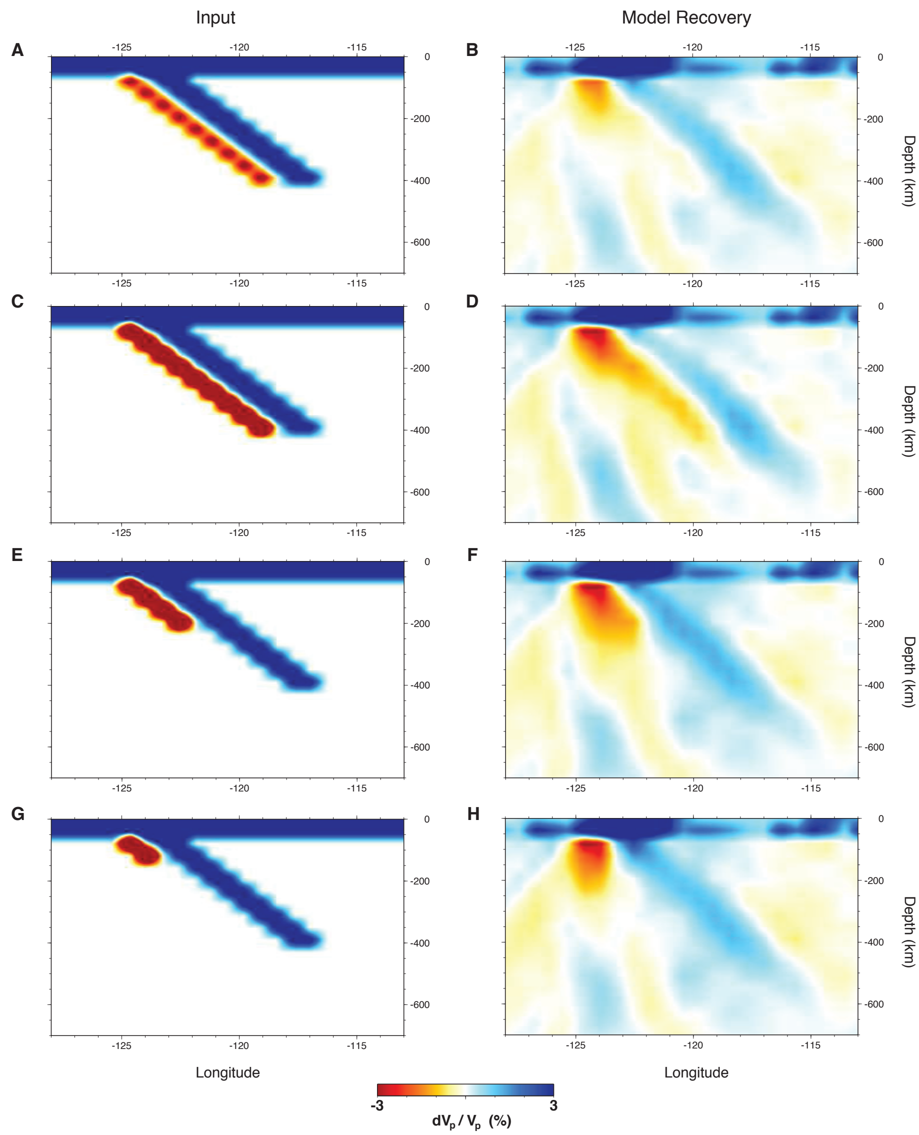

Fig. S8.

Synthetic models test optimal depths to which the low velocities can extend. All four models have an 80km-thick, +4% slab connected to a 60km-thick, +4% lithospheric lid that extends to the west. All four input low-velocity features are 30km thick. (**A**) The high-velocity slab is underlain by a –6% low-velocity feature that extends to 400km depth. (**B**) Recovery of the feature in the hinge is weaker than observed in CASC16-P, and sensitivity drops off rapidly with depth. (**C**) The slab is underlain by a –10% low-velocity feature that extends to 400km depth. (**D**) Signal in the hinge matches that observed in CASC16-P, but low velocities are recovered down to 400km depth, in contrast to CASC16-P. (**E**) The slab is underlain by a –10% low-velocity feature that extends to 200km depth. (**F**) Signal in the hinge is slightly stronger than that observed in CASC16-P, but the two are similar. The feature appears to extend down to 300km. (**G**) The slab is underlain by a –10% low-velocity feature that extends to 140km depth. (**H**) Signal in the hinge closely matches CASC16-P, and appears to extend down to 250km.

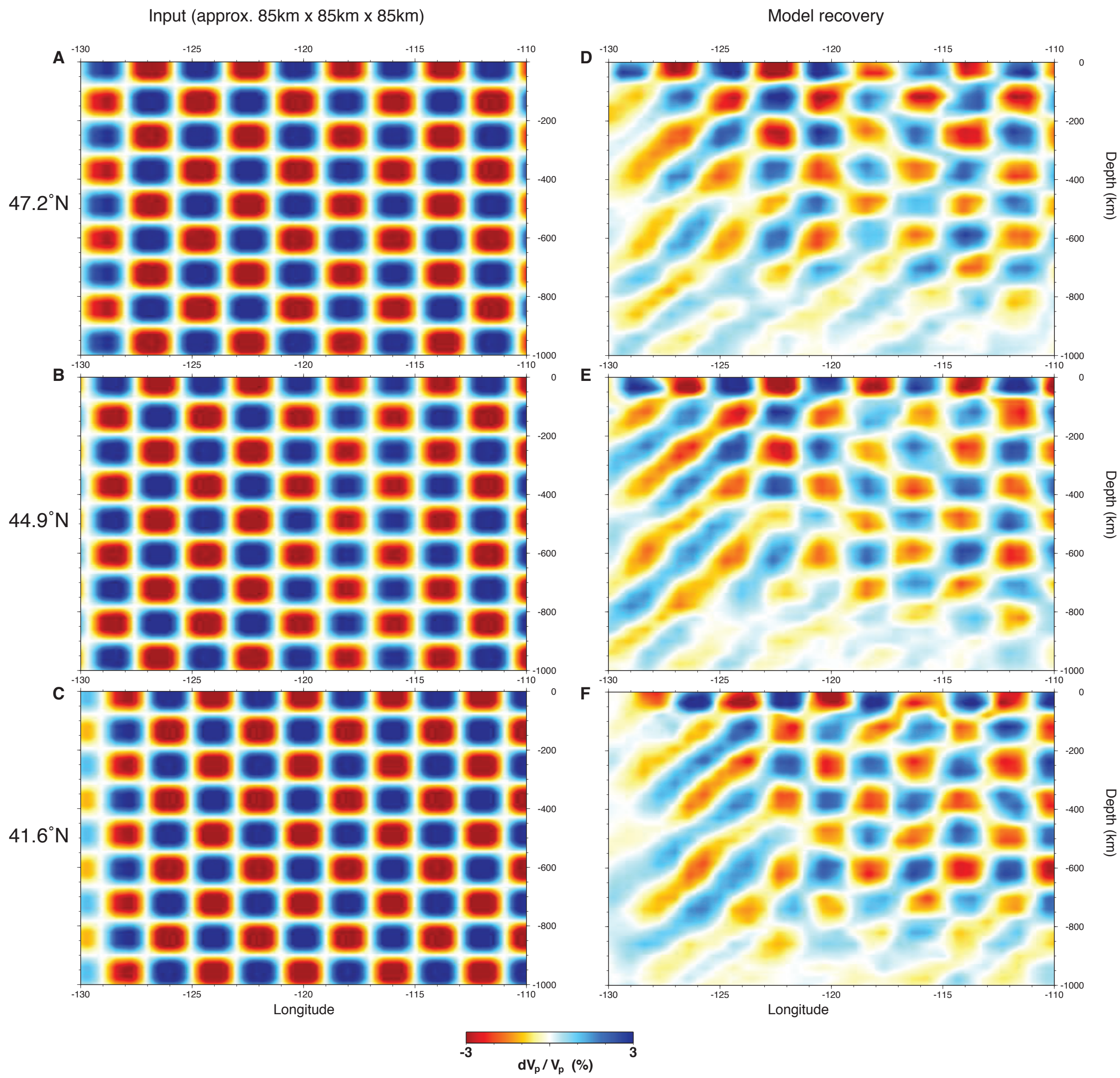

Fig. S9.

(**A–C**) Vertical slices at constant latitude through the input checkerboard velocity model. The boxes have anomalies of ±4%, and are approximately 85km per side at the surface, decreasing in size with depth. We have approximately 40km of 0% anomaly space between each cube. These synthetic anomalies were used to calculate synthetic travel-times, to which we add random noise by selecting randomly from a Gaussian distribution with a standard deviation of 15% of the travel-time delay. (**D–F**) slices through the recovered velocity structure show good recovery down to the transition zone east of –125° longitude. The slices also show little variation in resolution along the strike of the subduction zone.

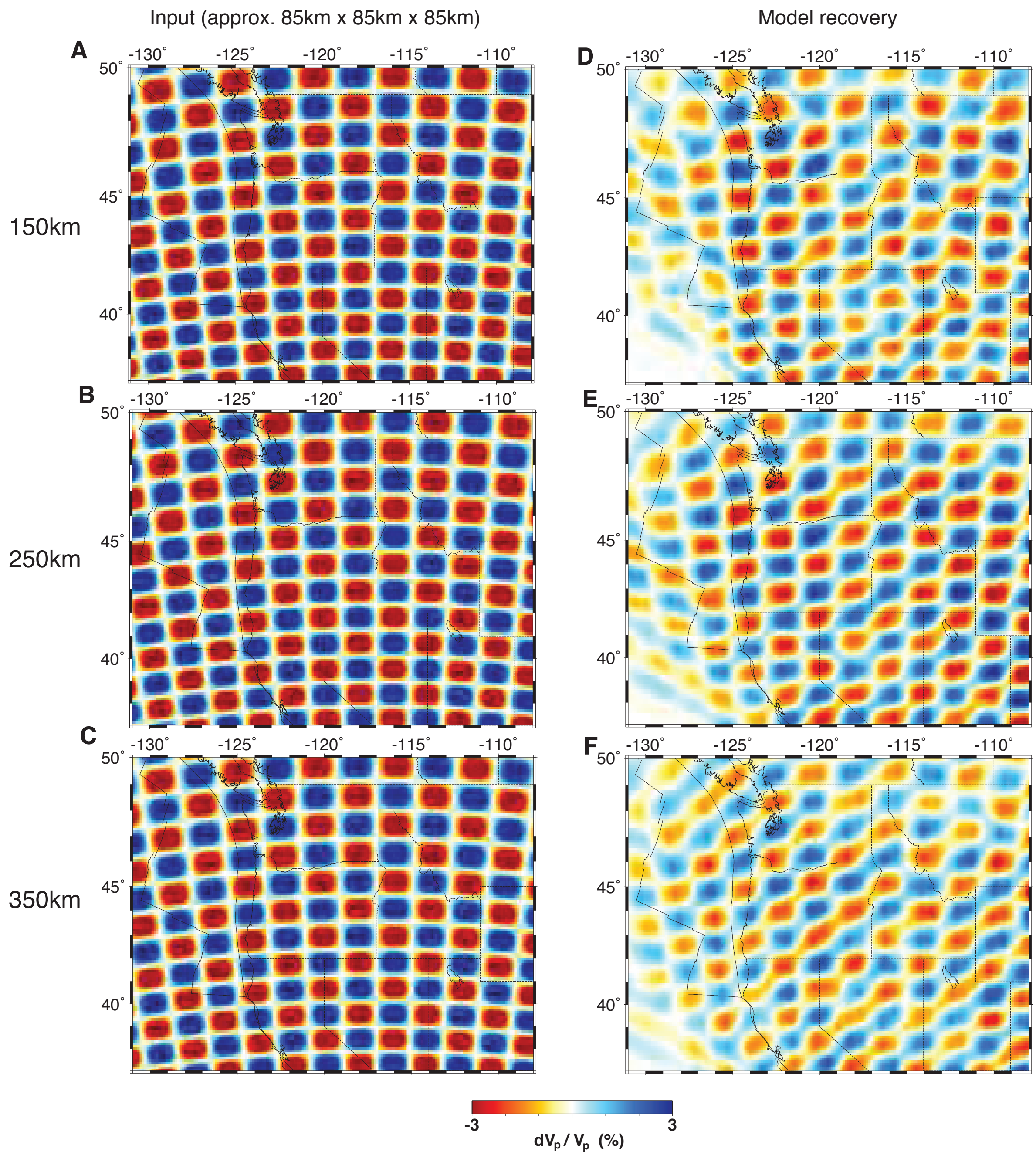

Fig. S10.

(**A–C**) Horizontal slices at constant depth through the input synthetic velocity model shown in Fig. S9. (**D–F**) Horizontal slices through the recovered velocity structure show good recovery through the majority of the model domain to 350km depth.

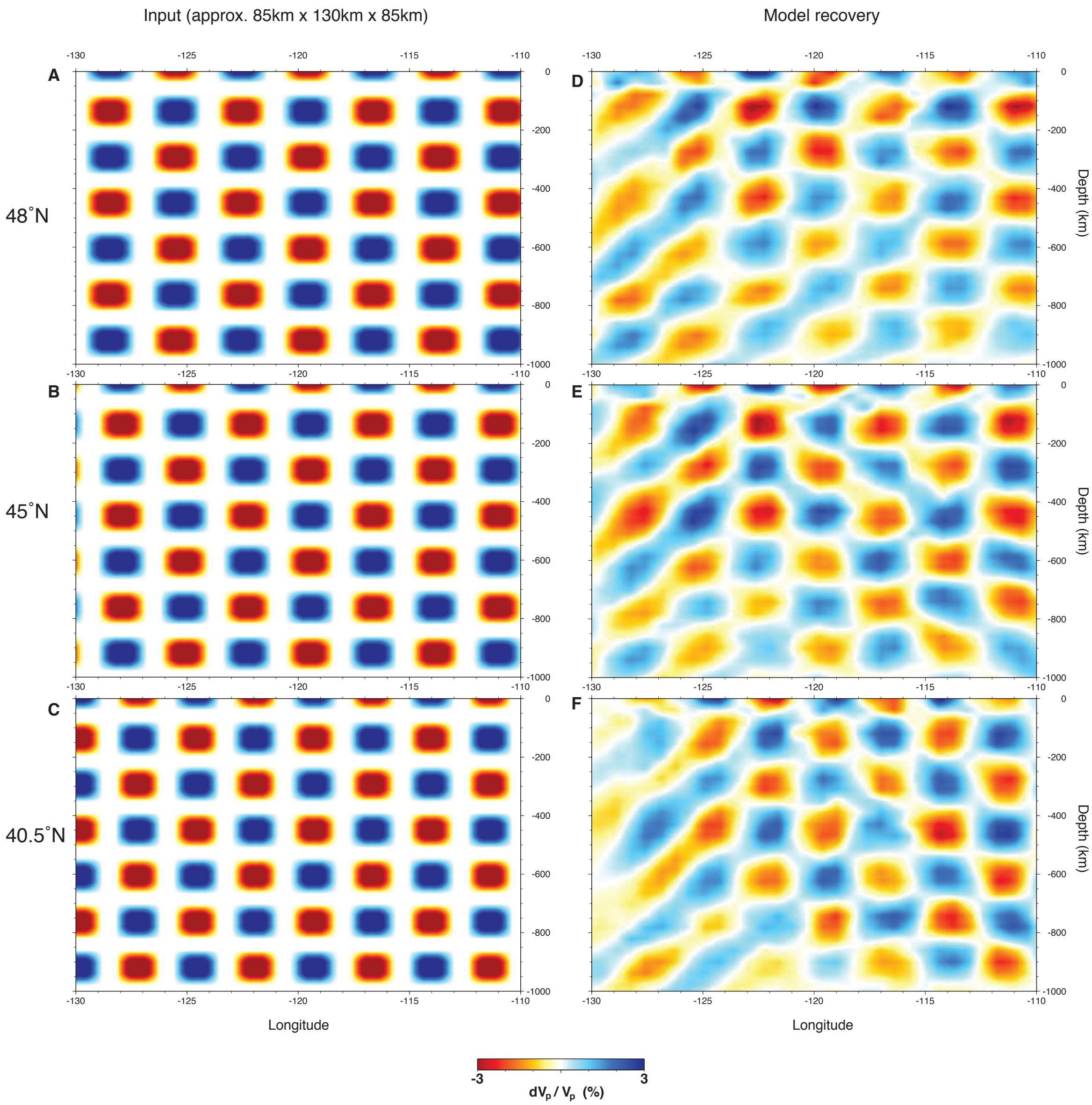

Fig. S11.

(**A–C**) Vertical slices at constant latitude through the input checkerboard velocity model. The boxes have anomalies of ±4%, and are approximately 85km vertically and east-to-west, and approximately 130km north-to-south at the surface, decreasing in size with depth. The boxes have approximately 85km of 0% anomaly space between them. These synthetic anomalies were used to calculate synthetic travel-times, to which we add random noise by selecting randomly from a Gaussian distribution with a standard deviation of 15% of the travel-time delay. (**D–F**) Slices through the recovered velocity structure show good recovery down to 700km east of –125° longitude.

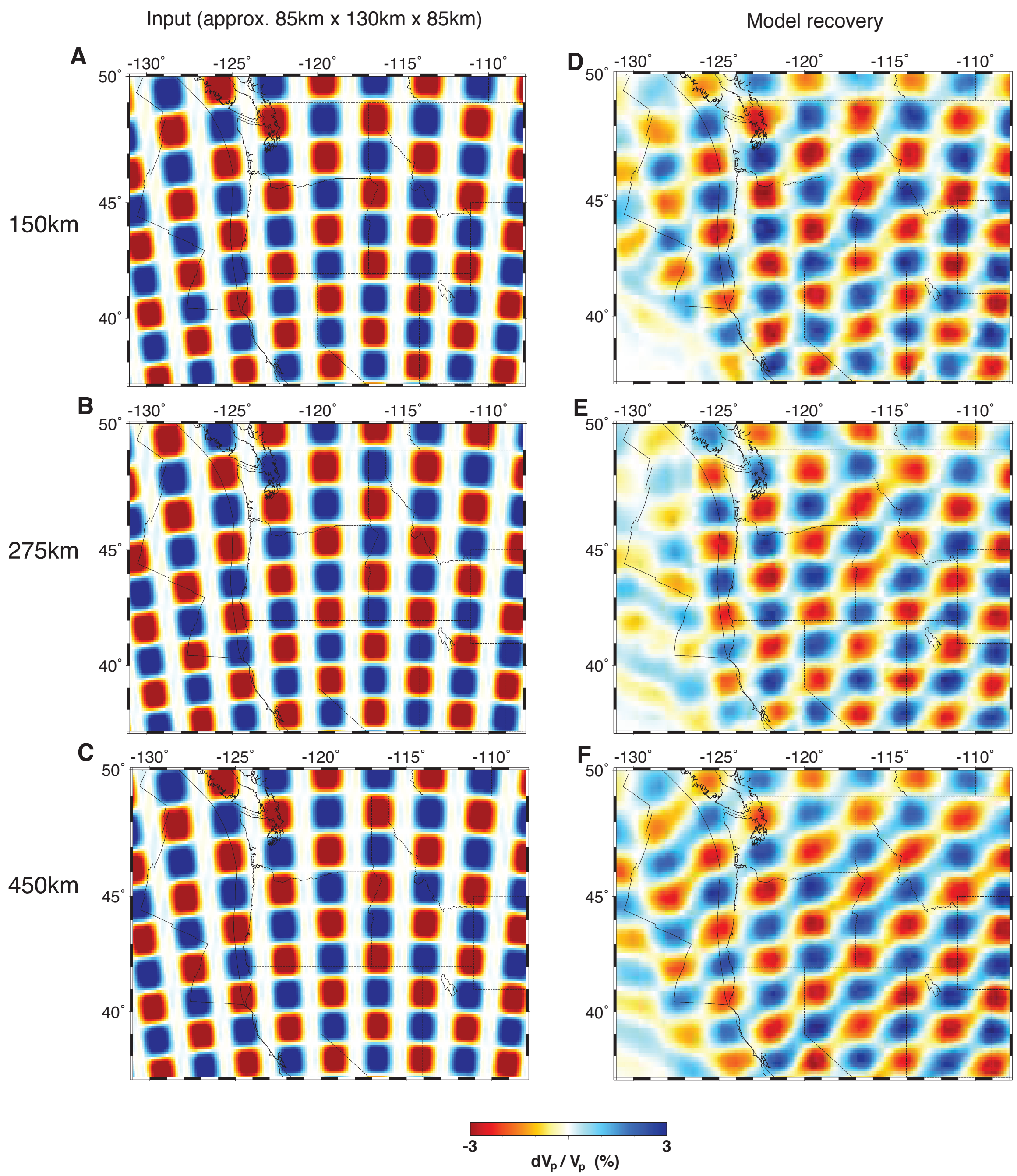

Fig. S12.

(**A–C**) Horizontal slices at constant depth through the input synthetic velocity model shown in Fig. S11. (**D–F**) Horizontal slices through the recovered velocity structure show good recovery through the majority of the model domain down to 450km depth.

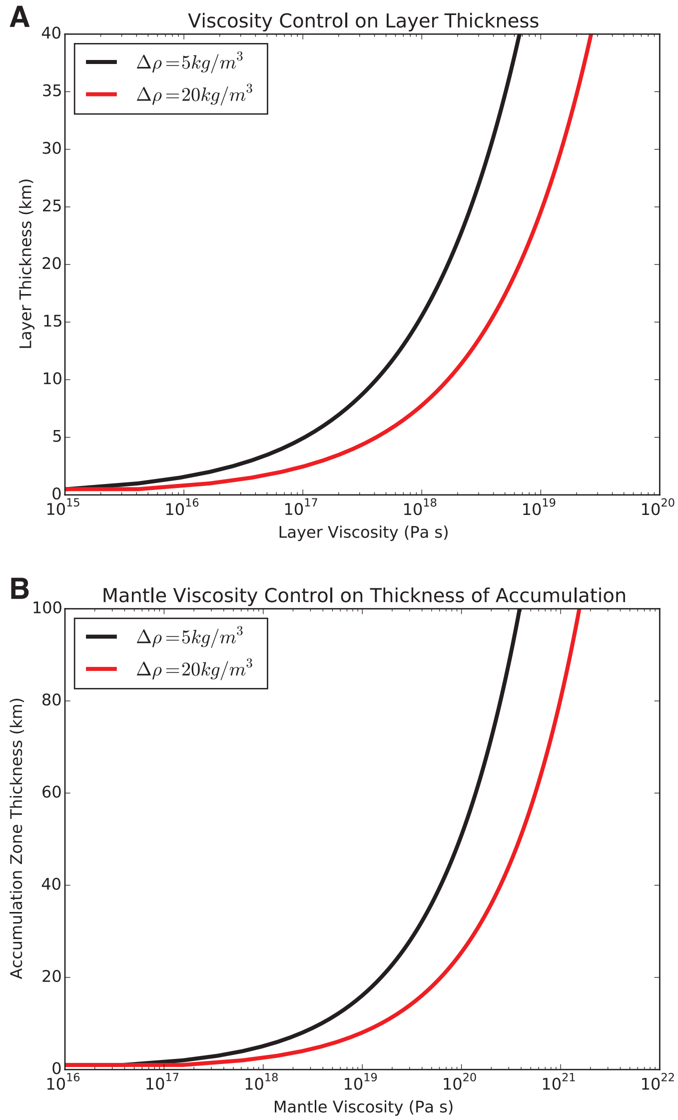

Fig. S13.

(**A**) Plot of the thickness of the horizontal layer h vs. its viscosity μ_l, from condition (1). For a layer thickness of 10–25km, the viscosity should fall in the range of $\sim 5\times10^{17} - 1\times10^{19}$ Pa-s. (**B**) Plot of the thickness of the accumulation zone H vs. the viscosity of the underlying mantle μ_m, from condition (2). For an accumulation zone thickness of 50–100km, the viscosity falls in the range of $\sim 1\times10^{20} - 1.1\times10^{21}$ Pa-s.

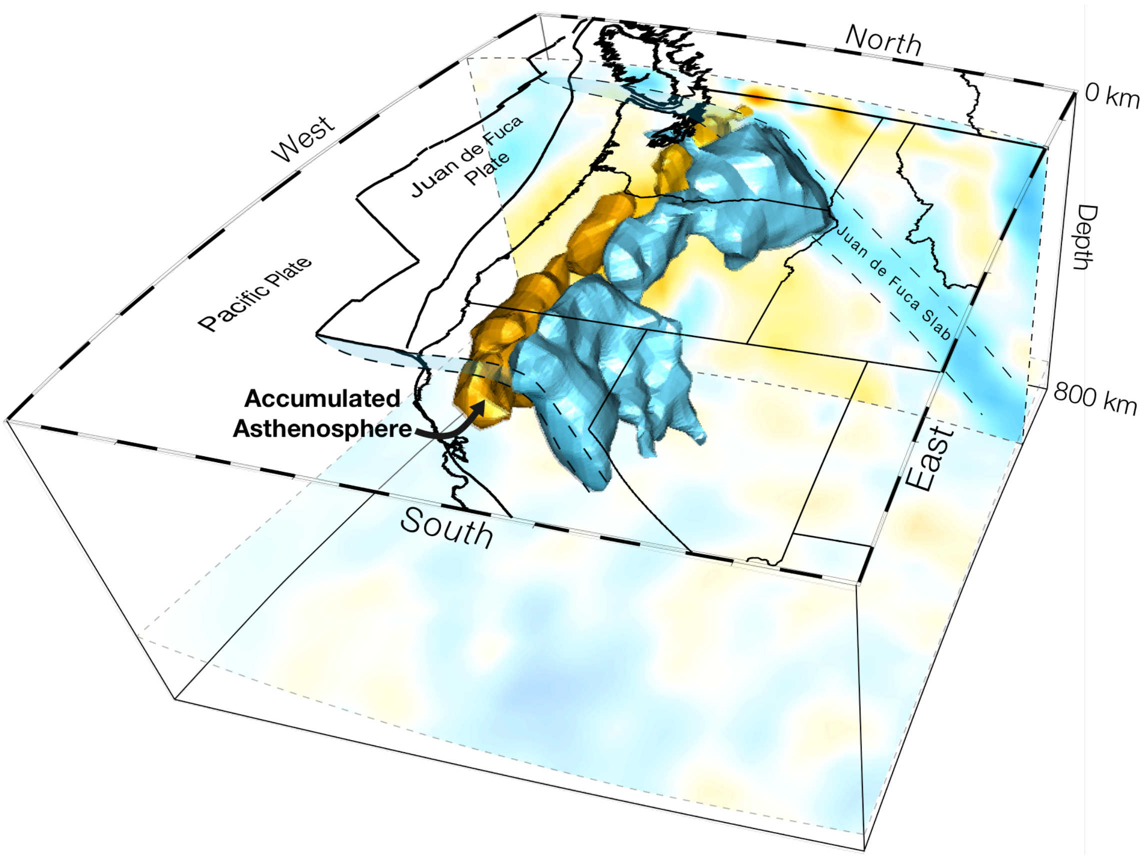

Fig. S14.

3D representation of the CASC16-P model. The box shows a volume from 36°N to 51°N, 112°W to 133°W, and 0 km to 800 km depth. A map showing political boundaries and tectonic plate boundaries is on the surface. A vertical slice at about 49°N shows the slab descending to depth, outlined by the dashed lines. The blue isosurface shows the high-velocity Juan de Fuca slab descending beneath the Pacific Northwest of the US. The orange isosurface to the west of the slab outlines the imaged low-velocity feature beneath the slab that we interpret as an accumulation of low-viscosity buoyant material.

References and Notes

1. M. A. Richards, W.-S. Yang, J. R. Baumgardner, H.-P. Bunge, Role of a low-viscosity zone in stabilizing plate tectonics: Implications for comparative terrestrial planetology. *Geochem. Geophys. Geosyst.* **2**, 1026 (2001). doi:10.1029/2000GC000115

2. C. H. Craig, D. McKenzie, The existence of a thin low-viscosity layer beneath the lithosphere. *Earth Planet. Sci. Lett.* **78**, 420–426 (1986). doi:10.1016/0012-821X(86)90008-7

3. K. M. Fischer, H. A. Ford, D. L. Abt, C. A. Rychert, The lithosphere-asthenosphere boundary. *Annu. Rev. Earth Planet. Sci.* **38**, 551–575 (2010). doi:10.1146/annurev-earth-040809-152438

4. C. A. Rychert, P. M. Shearer, A global view of the lithosphere-asthenosphere boundary. *Science* **324**, 495–498 (2009).doi:10.1126/science.1169754 Medline

5. H. Yuan, B. Romanowicz, K. M. Fischer, D. Abt, 3-D shear wave radially and azimuthally anisotropic velocity model of the North American upper mantle. *Geophys. J. Int.* **184**, 1237–1260 (2011). doi:10.1111/j.1365-246X.2010.04901.x

6. H. Kawakatsu, At the bottom of the oceanic plate. *Science* **335**, 1448–1449 (2012).doi:10.1126/science.1219658 Medline

7. T.-R. A. Song, H. Kawakatsu, Subduction of oceanic asthenosphere: Evidence from sub-slab seismic anisotropy. *Geophys. Res. Lett.* **39**, L17301 (2012). doi:10.1029/2012GL052639

8. M. D. Long, P. G. Silver, The subduction zone flow field from seismic anisotropy: A global view. *Science* **319**, 315–318 (2008).doi:10.1126/science.1150809 Medline

9. M. D. Long, P. G. Silver, Shear wave splitting and mantle anisotropy: Measurements, interpretations, and new directions. *Surv. Geophys.* **30**, 407–461 (2009). doi:10.1007/s10712-009-9075-1

10. D. Toomey, R. Allen, A. Barclay, S. Bell, P. Bromirski, R. Carlson, X. Chen, J. Collins, R. Dziak, B. Evers, D. Forsyth, P. Gerstoft, E. Hooft, D. Livelybrooks, J. Lodewyk, D. Luther, J. McGuire, S. Schwartz, M. Tolstoy, A. Trehu, M. Weirathmueller, W. Wilcock, The Cascadia Initiative: A sea change in seismological studies of subduction zones. *Oceanography* **27**, 138–150 (2014). doi:10.5670/oceanog.2014.49

11. M. Obrebski, R. M. Allen, M. Xue, S.-H. Hung, Slab-plume interaction beneath the Pacific Northwest. *Geophys. Res. Lett.* **37**, L14305 (2010). doi:10.1029/2010GL043489

12. B. Schmandt, E. Humphreys, Complex subduction and small-scale convection revealed by body-wave tomography of the western United States upper mantle. *Earth Planet. Sci. Lett.* **297**, 435–445 (2010). doi:10.1016/j.epsl.2010.06.047

13. Y. Tian, D. Zhao, P-wave tomography of the western United States: Insight into the Yellowstone hotspot and the Juan de Fuca slab. *Phys. Earth Planet. Inter.* **200-201**, 72–84 (2012). doi:10.1016/j.pepi.2012.04.004

14. R. W. Porritt, R. M. Allen, F. F. Pollitz, Seismic imaging east of the Rocky Mountains with USArray. *Earth Planet. Sci. Lett.* **402**, 16–25 (2014). doi:10.1016/j.epsl.2013.10.034

15. H. Kawakatsu, P. Kumar, Y. Takei, M. Shinohara, T. Kanazawa, E. Araki, K. Suyehiro, Seismic evidence for sharp lithosphere-asthenosphere boundaries of oceanic plates. *Science* **324**, 499–502 (2009).doi:10.1126/science.1169499 Medline

16. N. Schmerr, The Gutenberg discontinuity: Melt at the lithosphere-asthenosphere boundary. *Science* **335**, 1480–1483 (2012).doi:10.1126/science.1215433 Medline

17. S. Naif, K. Key, S. Constable, R. L. Evans, Melt-rich channel observed at the lithosphere-asthenosphere boundary. *Nature* **495**, 356–359 (2013).doi:10.1038/nature11939 Medline

18. T. A. Stern, S. A. Henrys, D. Okaya, J. N. Louie, M. K. Savage, S. Lamb, H. Sato, R. Sutherland, T. Iwasaki, A seismic reflection image for the base of a tectonic plate. *Nature* **518**, 85–88 (2015).doi:10.1038/nature14146 Medline

19. I. D. Bastow, Relative arrival-time upper-mantle tomography and the elusive background mean. *Geophys. J. Int.* **190**, 1271–1278 (2012). doi:10.1111/j.1365-246X.2012.05559.x

20. M. M. Hirschmann, Partial melt in the oceanic low velocity zone. *Phys. Earth Planet. Inter.* **179**, 60–71 (2010). doi:10.1016/j.pepi.2009.12.003

21. W. Zhu, G. A. Gaetani, F. Fusseis, L. G. J. Montési, F. De Carlo, Microtomography of partially molten rocks: Three-dimensional melt distribution in mantle peridotite. *Science* **332**, 88–91 (2011).doi:10.1126/science.1202221 Medline

22. G. Hirth, D. L. Kohlstedt, Water in the oceanic upper mantle: Implications for rheology, melt extraction and the evolution of the lithosphere. *Earth Planet. Sci. Lett.* **144**, 93–108 (1996). doi:10.1016/0012-821X(96)00154-9

23. R. L. Evans, P. E. Wannamaker, R. S. McGary, J. Elsenbeck, Electrical structure of the central Cascadia subduction zone: The EMSLAB Lincoln Line revisited. *Earth Planet. Sci. Lett.* **402**, 265–274 (2014). doi:10.1016/j.epsl.2013.04.021

24. D. L. Turcotte, G. Schubert, *Geodynamics* (Cambridge Univ. Press, 2002).

25. M. A. Feighner, M. A. Richards, The fluid dynamics of plume-ridge and plume-plate interactions: An experimental investigation. *Earth Planet. Sci. Lett.* **129**, 171–182 (1995). doi:10.1016/0012-821X(94)00247-V

26. S. Karato, H. Jung, Water, partial melting and the origin of the seismic low velocity and high attenuation zone in the upper mantle. *Earth Planet. Sci. Lett.* **157**, 193–207 (1998). doi:10.1016/S0012-821X(98)00034-X

27. C. Doglioni, A. Ismail-Zadeh, G. Panza, F. Riguzzi, Lithosphere–asthenosphere viscosity contrast and decoupling. *Phys. Earth Planet. Inter.* **189**, 1–8 (2011). doi:10.1016/j.pepi.2011.09.006

28. A. Paulson, M. A. Richards, On the resolution of radial viscosity structure in modelling long-wavelength postglacial rebound data. *Geophys. J. Int.* **179**, 1516–1526 (2009). doi:10.1111/j.1365-246X.2009.04362.x

29. T. Höink, A. Lenardic, Long wavelength convection, Poiseuille–Couette flow in the low-viscosity asthenosphere and the strength of plate margins. *Geophys. J. Int.* **180**, 23–33 (2010). doi:10.1111/j.1365-246X.2009.04404.x

30. N. Hirano, E. Takahashi, J. Yamamoto, N. Abe, S. P. Ingle, I. Kaneoka, T. Hirata, J. Kimura, T. Ishii, Y. Ogawa, S. Machida, K. Suyehiro, Volcanism in response to plate flexure. *Science* **313**, 1426–1428 (2006).doi:10.1126/science.1128235 Medline

31. U. Faul, I. Jackson, The seismological signature of temperature and grain size variations in the upper mantle. *Earth Planet. Sci. Lett.* **234**, 119–134 (2005). doi:10.1016/j.epsl.2005.02.008

32. A. H. Lachenbruch, J. H. Sass, Heat flow and energetics of the San Andreas Fault Zone. *J. Geophys. Res.* **85**, 6185–6222 (1980). doi:10.1029/JB085iB11p06185

33. J. A. Hole, B. C. Beaudoin, T. J. Henstock, Wide-angle seismic constraints on the evolution of the deep San Andreas plate boundary by Mendocino triple junction migration. *Tectonics* **17**, 802–818 (1998). doi:10.1029/98TC02261

34. K. P. Furlong, S. Y. Schwartz, Influence of the Mendocino triple junction on the tectonics of coastal California. *Annu. Rev. Earth Planet. Sci.* **32**, 403–433 (2004). doi:10.1146/annurev.earth.32.101802.120252

35. P. Wessel, W. H. F. Smith, R. Scharroo, J. Luis, F. Wobbe, Generic Mapping Tools: Improved version released. *Eos* **94**, 409–410 (2013). doi:10.1002/2013EO450001

36. P. A. McCrory, J. L. Blair, F. Waldhauser, D. H. Oppenheimer, Juan de Fuca slab geometry and its relation to Wadati-Benioff zone seismicity. *J. Geophys. Res.* **117**, B09306 (2012). doi:10.1029/2012JB009407

37. S. C. Webb, Broadband seismology and noise under the ocean. *Rev. Geophys.* **36**, 105–142 (1998). doi:10.1029/97RG02287

38. B. T. R. Lewis, L. M. Dorman, Recording teleseisms on the seafloor; an example from the Juan de Fuca plate. *Bull. Seismol. Soc. Am.* **88**, 107–116 (1998).

39. J. C. VanDecar, R. S. Crosson, Determination of teleseismic relative phase arrival times using multi-channel cross-correlation and least squares. *Bull. Seismol. Soc. Am.* **80**, 150–169 (1990).

40. S.-H. Hung, F. A. Dahlen, G. Nolet, Fréchet kernels for finite-frequency traveltimes—II. Examples. *Geophys. J. Int.* **141**, 175–203 (2000). doi:10.1046/j.1365-246X.2000.00072.x

41. F. A. Dahlen, S.-H. Hung, G. Nolet, Fréchet kernels for finite-frequency traveltimes—I. Theory. *Geophys. J. Int.* **141**, 157–174 (2000). doi:10.1046/j.1365-246X.2000.00070.x

42. S.-H. Hung, Y. Shen, L.-Y. Chiao, Imaging seismic velocity structure beneath the Iceland hot spot: A finite frequency approach. *J. Geophys. Res.* **109**, B08305 (2004). doi:10.1029/2003JB002889